Nano Research
2022, 15(10): 9223–9233

ISSN 1998-0124 CN 11-5974/O4
https://doi.org/10.1007/s12274-022-4599-5

Research Article

Integrating Au and ZnO nanoparticles onto graphene nanosheet for enhanced sonodynamic therapy

Fei Wang[1], Boyu Wang[2], Wei You[2], Guang Chen[2] (✉), and Ye-Zi You[2] (✉)

[1] *Neurosurgical Department, the First Affiliated Hospital of USTC, Division of Life Sciences and Medicine, University of Science and Technology of China, Hefei 230001, China*
[2] *Department of Polymer Science and Engineering, University of Science and Technology of China, Hefei 230026, China*

Received: 29 March 2022 / **Revised:** 22 May 2022 / **Accepted:** 28 May 2022

ABSTRACT

Sonodynamic therapy has attracted widespread attention for cancer treatment because of its noninvasiveness and high tissue-penetration ability. Generally, ultrasound irradiation of sonosensitizers produces separated electrons (e^-) and holes (h^+), which inhibits cancer by producing reactive oxygen species (ROS). However, the separated electrons (e^-) and holes (h^+) could easily recombine, lowering the yield of ROS and hindering the application of sonodynamic therapy (SDT). Herein, we present a highly efficient sonosensitizer system for enhanced sonodynamic therapy built on reduced graphene oxide (rGO) nanosheets, bridged ZnO and Au nanoparticles, coated with polyvinyl pyrrolidone (PVP). The ultrasound irradiation activates ZnO nanoparticles to generate separated electron–hole (e^-–h^+) pairs, and the rGO nanosheets facilitate electron transfer from ZnO to Au nanoparticles because of the narrow band gap of rGO, which could efficiently restrain the recombination of the e^-–h^+ pairs, thereby significantly augmenting the production of ROS to kill cancer cells, such as U373MG, HeLa, and CT26 cells. Moreover, rGO nanosheets integrated with Au nanoparticles could catalyze the endogenous decomposition of H_2O_2 into O_2, which can alleviate hypoxic tumor microenvironment (TME). Therefore, the rational design of Au-rGO-ZnO@PVP nanomaterials can not only improve the efficiency of sonodynamic therapy, but also mitigate the hypoxic tumor microenvironment, which would provide a new perspective in the development of efficient sonosensitizers.

KEYWORDS

sonodynamic therapy, reactive oxygen species, reduced graphene oxide, tumor

1 Introduction

Cancer, as one of the most severe diseases in global public health issues, is the second leading cause of deaths worldwide [1]. Compared to traditional treatments (e.g., surgery, radiotherapy, and chemotherapy), reactive oxygen species (ROS)-based cancer therapy, such as the photodynamic therapy (PDT), has been widely researched in past decade because of its minimal invasiveness, which prevents painful therapy and severe side effects of traditional procedures [2]. However, their scant tissue penetration depth and inherent phototoxicity severely hindered the clinical application of PDT [3–9]. Strategies to eliminate cancer more effectively have therefore gained widespread attention.

Ultrasound (US) is a mechanical wave with a very short wavelength, which has been widely used in clinical surgery and diagnosis due to its high tissue-penetrating ability, non-invasiveness, and controllability [10]. Because of these properties, sonodynamic therapy (SDT) induced by US irradiation was considered as an alternative treatment to PDT [11–15]. In recent years, many sonosensitizers have been reported, such as Rose Bengal, porphyrin derivatives, zinc oxide (ZnO), etc. [11–13, 15–17]. Compared to traditional organic sonosensitizers, inorganic nanomaterials, for instance titanium dioxide, zinc oxide, and their functional nanocomposites, have become splendid candidates for sonosensitizers owing to their unparalleled chemical and physical characters [18–22]. Due to their excellent biocompatibility, tumor accumulation ability, and chemical stability, studies about inorganic sonosensitizers have substantially accelerated the application of SDT for cancer therapy. Generally, ultrasound irradiation can activate inorganic sonosensitizers to generate electron–hole (e^-–h^+) pairs with the ability of subsequent ROS generation [23–25]. However, the produced e^-–h^+ pairs could recombine very quickly, which highly hinders their further biomedical development and clinical application [18, 21–24]. Hence, methods to inhibit e^-–h^+ pair recombination is critical to increasing the efficiency of SDT based on inorganic sonosensitizers [16, 19, 20].

Recently, Cao et al. synthesized Au-TiO_2 nanosheets by decorating Au nanocrystals on the (001) active facet edge of TiO_2 nanosheets to promote the interfacial electrons transferring in the composite for enhanced SDT [18]. However, the ROS yield of Au-TiO_2 nanosheets was still limited. Dai et al. found that the two-dimensional (2D) graphene decorated with TiO_2 could separate the e^-–h^+ pairs and prevent their fast recombination upon external US activation to improve the SDT efficiency against tumors [24]. However, due to the limited efficiency of e^-–h^+ pair separation, this strategy still needs long-time US irradiation and combines with PDT, which will limit the further application of SDT.

Address correspondence to Guang Chen, cg1995@mail.ustc.edu.cn; Ye-Zi You, yzyou@ustc.edu.cn

Here, we propose the use of reduced graphene oxide (rGO) nanosheets as a bridge for integrating ZnO and Au nanoparticles due to its very narrow band gap. In this case, the ultrasound irradiation activates ZnO to generate separated e^-–h^+ pairs, and the rGO nanosheets facilitate electron transfer from ZnO nanoparticles to Au nanoparticles, thereby efficiently preventing the fast recombination of the electrons and holes. Hence, this strategy could enhance the quantum yield of ROS generation and improve the efficiency of sonodynamic therapy. Moreover, because of the high metabolism of tumor cells and the deficient oxygen provision, the level of hydrogen peroxide (H_2O_2) in tumors is excessive. Here, rGO nanosheets integrated with Au nanoparticles can act as a catalyst to effectively convert the excess H_2O_2 into O_2 and alleviate the hypoxic tumor microenvironment (TME), which can subsequently enhance ROS generation [26, 27]. Hence, Au-rGO-ZnO@PVP nanomaterials can enhance the efficiency of sonodynamic therapy through two aspects: (i) inhibiting the fast recombination of e^-–h^+ pairs and (ii) alleviating the hypoxia-associated barrier. This ingenious design provides a novel strategy for augmenting the SDT efficiency of semiconductor ZnO-based sonosensitizers, which can promote the further clinical application of sonodynamic therapy.

2 Experimental section

2.1 Materials

Zinc acetate dihydrate ($Zn(CH_3COO)_2$, 99%), polyvinyl pyrrolidone (PVP, K30), and tetramethylammonium hydroxide pentahydrate (97%) were purchased from Sinopharm Chemical Reagent Co., Ltd. Graphene oxide (GO, 98%) was purchased from Shanghai Yuanye Bio-Technology Co., Ltd. 2,2,6,6-Tetramethylpiperidine (TEMP, 99%), 5,5-dimethyl-1-pyrrolidine-N-oxide (DMPO, 99%), and 1,3-diphenylisobenzofuran (DPBF, 98%) were brought from Aladdin. Oleic acid (99%) and Rhodamine B (RhB, 99%) were purchased from Macklin Chemical Co., Ltd. Tris(4,7-diphenyl-1,10-phenanthroline) ruthenium(II) dichloride complex ($Ru(dpp)_3Cl_2$, 98%) and methylthiazolyldiphenyltetrazolium bromide (MTT) were purchased from Sigma-Aldrich. Dulbecco's modified Eagle's medium (DMEM), fetal bovine serum (FBS), phosphate buffer saline (PBS), Calcein-AM, propidium iodide (PI), and reactive oxygen species assay kit were obtained from Beyotime Biotechnology Co., Ltd.

2.2 Characterization

A JEM-2100F high-resolution transmission electron microscope was used to observe the sizes and morphologies of the nanomaterials. Size and zeta potential measurements were conducted on a Nano Brook 90Plus PALS Zetasizer system. The corresponding energy dispersive X-ray spectroscopy (EDS) was acquired on a Gemini SEM 500 electron microscope operated at 200 kV. The quantitative analysis of each element content in the nanomaterials was obtained by inductively coupled plasma-optical emission spectrometry (ICP-OES) (Optima 7300 DV). The Fourier transform infrared spectra (FTIR) of the samples were recorded using a Thermo Fisher Nicolet 6700 FTIR spectrometer. A Shimadzu UV-3600 ultraviolet–visible–near infrared (UV–vis–NIR) spectrophotometer was used to record UV–vis–NIR adsorption spectra. The photoluminescence (PL) spectra were measured on the fluorescence spectrophotometer (F-4600). A JEOL JES-FA200 electron paramagnetic resonance spectrometer was used to characterize the electron spin resonance (ESR) signal of singlet oxygen ($^1O_2$) and hydroxyl radical (·OH). An Olympus IX71 fluorescence microscope was used to carry out the fluorescence imaging. A Fluorescence Activating Cell Sorter (BD FACS Calibur) was used for flow cytometry analysis.

2.3 Synthesis of ZnO nanoparticles

Oleate-capped ZnO nanoparticles were prepared as previously published report [28]. Zinc acetate dihydrate (526.0 mg, 1.2 mmol) was dissolved in ethanol (40 mL) at a temperature under 50 °C. After adding oleic acid (170 μL, 0.53 mmol), the solution was heated to reflux under vigorous magnetic stirring. Then, 10 mL ethanol solution containing tetramethylammonium hydroxide pentahydrate (720 mg, 3.97 mmol) was added into the solution with $Zn(CH_3COO)_2$ and oleic acid, and the mixture was refluxed for an additional 30 min. After cooling the system to room temperature, the produced turbid solution of ZnO nanoparticles was centrifuged (5 min at 7,000 rpm) and washed with ethanol 3 times (yield: 78%).

2.4 Synthesis of Au-rGO-ZnO, ZnO-rGO, Au-rGO, Au-rGO-$ZnO_{0.5}$, and $Au_{0.5}$-rGO-ZnO nanomaterials

GO nanosheet dispersion was collected after probe-sonication for 4 h and centrifugation at 10,000 rpm. $HAuCl_4$ aqueous solution (2.0 mg/mL, 5.0 mL) was added into 30 mL of GO nanosheet dispersion (0.67 mg/mL) and stirred for 30 min at room temperature to a yellow-brown solution. Subsequently, oleate-capped ZnO nanoparticles (40 mg) dispersed in toluene (45 mL) were added into the yellow-brown solution, and the mixture was kept rapidly stirring for 5 h at room temperature. After adding 20.0 μL of hydrazine hydrate, the mixture was stirred for another 8 h at 80 °C, and the color of the suspension changed to purple, forming rGO nanosheets integrated with Au and ZnO nanoparticles. Typically, when the mass ratio of GO:$HAuCl_4$:ZnO was kept at 2:0:4, 2:1:0, 2:1:2, and 2:0.5:4, the as-prepared nanomaterials were denoted as ZnO-rGO, Au-rGO, Au-rGO-$ZnO_{0.5}$, and $Au_{0.5}$-rGO-ZnO, respectively. Finally, the as-prepared nanomaterials were washed with large amounts of acetone and centrifuged for 10 min at 7,000 rpm three times (yield: 55%).

2.5 Synthesis of Au-rGO-ZnO@PVP nanomaterials

To improve their stability in the physiological environment, Au-rGO-ZnO nanomaterials were decorated with PVP. Au-rGO-ZnO nanomaterials (30 mg) and PVP (K30, 120.0 mg) were dissolved in dimethylformamide (DMF, 60 mL), and the mixture was added into a round-bottom flask, which was vigorously stirred at 80 °C for 12 h. The resulting Au-rGO-ZnO@PVP nanomaterials were collected by centrifugation and washing with ethanol for several times to remove unattached PVP. The as-prepared Au-rGO-ZnO@PVP nanomaterials were finally dissolved in PBS (pH = 7.4) and stored at the room temperature for further use.

2.6 O_2 generation via the decomposition of H_2O_2

The O_2 generation of ZnO and Au-rGO-ZnO@PVP by decomposing H_2O_2 was examined with an oxygen probe (JPB-70A portable dissolved oxygen meter). Briefly, ZnO and Au-rGO-ZnO@PVP (100 μg/mL) were dissolved in anaerobic water containing 1 mM H_2O_2, respectively, and the O_2 production was detected with time under US irradiation (1 MHz, 1.0 W/cm^2, 50% cycle).

2.7 ESR spectra test

TEMP and DMPO were used to examine the generation of $^1O_2$ and ·OH produced by ZnO, ZnO-rGO@PVP, and Au-rGO-ZnO@PVP. Typically, 10.0 μL of TEMP was added into 2.5 mL suspensions of ZnO, ZnO-rGO@PVP or Au-rGO-ZnO@PVP

solutions (100 μg/mL). Then, these suspensions were respectively exposed to US irradiation (1.0 MHz, 1.0 W/cm^2, 50% duty cycle) for 90 s. The $^1O_2$ signals were immediately monitored by the electron paramagnetic resonance spectrometer. In addition, the suspensions containing ZnO, ZnO-rGO@PVP or Au-rGO-ZnO@PVP (100 μg/mL) were mixed with DMPO (5 μL), respectively, which were followed with US irradiation (1.0 MHz, 1.0 W/cm^2, 50% duty cycle) for 90 s. DMPO trapped ·OH, and the signals of ·OH were further detected with the electron paramagnetic resonance spectrometer.

2.8 ROS generation under US irradiation

DPBF was used to detect $^1O_2$ production, and RhB was used to evaluate ·OH generation. Briefly, DPBF (60 μM, 15.0 μL) or RhB (2 mM, 25.0 μL) dissolved in DMF was added to 2.5 mL of ZnO, ZnO-rGO@PVP, and Au-rGO-ZnO@PVP suspensions (100 μg/mL). Then, these mixtures were exposed to US irradiation (1.0 MHz, 1.0 W/cm^2, 50% duty cycle) in the dark. Finally, the changes in either DPBF or RhB were traced by measuring the absorption intensity in UV–vis–NIR spectrometer.

2.9 Cell culture

HeLa human cervical cancer cells (noted as HeLa cells) and CT26 murine colon cancer cells (noted as CT26 cells) were used for following *in vitro* experiments and CT26 cells were used for *in vivo* evaluations. Both cell lines were purchased from Beyotime Biotechnology Co., Ltd. and cultured at 37 °C under 5% CO_2 in DMEM (high glucose, GIBCO) supplemented with 10% FBS (GIBCO) and 1% penicillin/streptomycin.

2.10 *In vitro* cytotoxicity of Au-rGO-ZnO@PVP nanomaterials by MTT assay

For cell viability measurements, HeLa and CT26 cells (1×10^4 cells/well) were seeded into 96-well cell culture plates until adherent, separately, and then co-incubated for 24 h with Au-rGO-ZnO@PVP at different concentrations (0, 12.5, 25, 50, 75, and 100 μg/mL). Subsequently, the relative cell viabilities were evaluated by a standard MTT assay. In brief, after co-incubation, DMEM (100 μL per well) containing MTT (1.0 mg/mL) was used to replace the culture medium and cultured for another 4 h. Finally, the DMEM was replaced with dimethyl sulfoxide (DMSO, 150 μL per well) and shaken for 10 min to dissolve purple formazan, and the viability of cells was detected by using a microplate reader at both 490 and 570 nm. Cell viability was calculated by comparing with the absorbance of the cells in control group and expressed as the percentage histogram.

2.11 *In vitro* sonodynamic therapy against cancer cells by Au-rGO-ZnO@PVP nanomaterials

For testing the SDT efficacy of Au-rGO-ZnO@PVP, both HeLa and CT26 cells were seeded into 96-well cell culture plates (1×10^4 cells/well) until adherent, and then co-incubated with ZnO, ZnO-rGO@PVP, and Au-rGO-ZnO@PVP (50 μg/mL) separately for 24 h. Then, these cells were treated with US irradiation (1.0 MHz, 1.0 W/cm^2, 50% duty cycle) for 2 min and incubated for another 24 h. After incubation, DMEM (100 μL per well) containing MTT (1.0 mg/mL) was used to replace the culture medium and cultured for another 4 h. The DMEM was then replaced with DMSO (100 μL per well) and shaken for 10 min to dissolve purple formazan. Finally, a microplate reader was used to measure the absorbance at both 490 nm and 570 nm of each well. Cell viability was calculated by comparing with the absorbance of the cells in control group and expressed as the percentage histogram.

2.12 Apoptosis test using Calcein-AM/PI staining

HeLa and CT26 cells were seeded into 96-well cell culture plates (1×10^4 cells/well), separately, cultured in DMEM supplemented with 10% FBS overnight, and then co-incubated with ZnO, ZnO-rGO@PVP, and Au-rGO-ZnO@PVP (50 μg/mL) separately for 24 h. These cells were treated with different groups, including PBS only group, PBS + US group, ZnO only group, ZnO + US group, ZnO-rGO@PVP only group, ZnO-rGO@PVP + US group, Au-rGO-ZnO@PVP only group, and Au-rGO-ZnO@PVP + US group. The parameters of US were set as 1.0 MHz, 1.0 W/cm^2, and 50% duty cycle. Finally, these cells were stained with Calcein-AM and PI following the protocol of the manufacturer (Beyotime Biotechnology Co., Ltd.). After staining for 20 min, these cells were washed 3 times with PBS (pH = 7.4) and inspected by fluorescence microscopy.

2.13 *In vitro* cellular ROS generation

To verify intracellular ROS production, the HeLa cells and CT26 cells (1×10^4 cells/well) were seeded into 96-well cell culture plates until adherent, separately, and co-incubated with ZnO, ZnO-rGO@PVP, and Au-rGO-ZnO@PVP separately at 37 °C in humidified 5% CO_2 for 24 h. Then, the cell culture medium was replaced with the 2′,7′-dichlorofluorescein diacetate (DCFH-DA) solution following the protocol of the manufacturer (Beyotime Biotechnology Co., Ltd.) and co-incubated for 30 min in the dark. After co-incubation, these cells were washed with PBS (pH = 7.4) 3 times to remove the remaining DCFH-DA. Finally, after US irradiation (1.0 MHz, 1.0 W/cm^2, 50% duty cycle) for 2 min, these cells were observed by fluorescence microscope and collected for flow cytometry analysis.

2.14 *In vitro* cellular mitigation of hypoxic tumor microenvironment

HeLa and CT26 cells were seeded into two 96-well plates (1×10^4 cells/well), separately, which were treated as two groups (hypoxic group and normoxic group). After incubated for 24 h until adherent, these cells were co-incubated with Au-rGO-ZnO@PVP (50 μg/mL) and H_2O_2 (50 μM) for another 24 h. Then, after treated under US irradiation (1.0 MHz, 1.0 W/cm^2, 50% duty cycle) for 2 min, the tris(4,7-diphenyl-1,10-phenanthroline) ruthenium dichloride complex solution (10 μg/mL) was added into each well and co-incubated for 1 h. Finally, these cells were gently washed with PBS (pH = 7.4) 3 times and inspected with fluorescence microscope.

2.15 *In vivo* treatments

Female Balb/c mice (5 weeks) were purchased from Shanghai SLAC Laboratory Animal Co., Ltd, and the animal study protocol was approved by the Institutional Animal Care and Use Committee at the University of Science and Technology of China. To establish the animal models, CT26 cells (2×10^6 cells) were subcutaneously injected into the back of each female Balb/c mouse. CT26 tumor-bearing mice were randomly divided into six groups (n = 5, each group): (1) control group (intratumorally injected with PBS only); (2) US only group (treated with US irradiation); (3) Au-rGO-ZnO@PVP only group (intratumorally injected with Au-rGO-ZnO@PVP only); (4) ZnO + US group (intratumorally injected with ZnO followed by US irradiation); (5) ZnO-rGO@PVP + US group (intratumorally injected with ZnO-rGO@PVP under US irradiation); (6) Au-rGO-ZnO@PVP + US group (intratumorally injected with Au-rGO-ZnO@PVP under US irradiation). The injection dose of different groups was 2.5 mg/kg. 4 h after intratumoral (i.t.) injection, these above therapeutic schedules were treated with US irradiation (1.0 MHz,

1.0 W/cm², 50% duty cycle) for 4 min and repeated on the fourth day during the therapeutic process. The body weights and tumor dimensions were surveyed by a caliper and noted every two days. The tumor volumes were calculated by volume = (length × width²)/2. These tumors were collected and sliced for further staining by hematoxylin and eosin (H&E) and terminal deoxynucleotidyl transferase-mediated dUTP-biotin nick end labeling (TUNEL) to observe the structure and status of cells for evaluating the efficiency of SDT.

2.16 *In vivo* toxicity assessment

After two weeks of treatment, mice were euthanized and then the main organs (heart, liver, spleen, lung, and kidney) were collected for H&E staining. The healthy female Balb/c mice were randomly divided into two groups (n = 5, each group): (1) control group (intravenously injected with PBS only); (2) Au-rGO-ZnO@PVP group (intravenously injected with Au-rGO-ZnO@PVP). Before mice were euthanatized, blood samples were collected for complete blood panel analyses and serum biochemistry test including liver functions and renal functions. Furthermore, for long-time toxicity experiment, healthy female Balb/c mice were divided into six groups by using the above therapeutic schedule to treat. During the 52-day treatment, the survival rates of these Balb/c mice were recorded every two days.

2.17 *In vivo* ROS staining

For fluorescence staining for tumoral ROS: After different nanomaterials were intratumorally injected, these mice were injected with DCFH-DA (3 mg/kg) intraperitoneally, then treated with or without US irradiation (1.0 MHz, 1.0 W/cm², 50% duty cycle) for 4 min. The tumors were surgically excised and the frozen tumor slices were prepared, and the fluorescence images were obtained to evaluate the production of ROS.

3 Results and discussion

3.1 Synthesis and characterization of Au-rGO-ZnO@PVP nanomaterials

In this work, ZnO nanoparticles were prepared as previously reported methods [28, 29]. In order to obtain Au-rGO-ZnO nanomaterials, GO nanosheets and $HAuCl_4$ were reduced to rGO nanosheets and Au nanoparticles by hydrazine hydrate, respectively. Subsequently, ZnO nanoparticles were added and integrated onto the rGO via electrostatic interaction between rGO and ZnO, forming Au-rGO-ZnO. Finally, biocompatible PVP was linked onto the surface of Au-rGO-ZnO nanomaterials via the π–π interaction through PVP and rGO (Au-rGO-ZnO@PVP) for enhancing the physiological stability (Fig. 1(a)). Transmission electron microscopy (TEM) was used to image the shape and structure of Au-rGO-ZnO@PVP nanomaterials. As shown in Figs. 2(a) and 2(b), the 2D planar size of rGO nanosheets was about 300 nm, and both Au nanoparticles and ZnO nanoparticles with size of ~ 5 nm were integrated onto the rGO surface, forming Au-rGO-ZnO@PVP nanomaterials with size of ~ 300 nm (Fig. 2(c)). The element distribution mapping of Zn and Au elements exhibited the ZnO nanoparticles and Au nanoparticles distribution on rGO nanosheets evenly, verifying the successful integration of ZnO nanoparticles and Au nanoparticles on the rGO nanosheets (Fig. 2(d)). In addition, as shown in Fig. 2(e), the wide absorption peaks at 489 cm⁻¹ of both Au-rGO-ZnO and Au-rGO-ZnO@PVP were attributed to the Zn–O stretching vibration [30, 31]. Meanwhile, according to the ICP-OES, the quality percent of Au and ZnO in Au-rGO-ZnO@PVP is 5.93% and

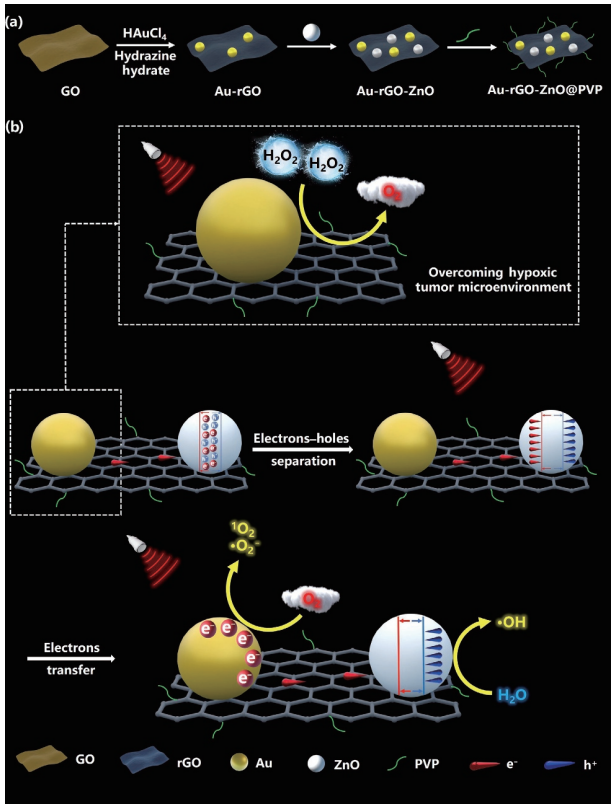

Figure 1 Schematic diagram of Au-rGO-ZnO@PVP nanomaterials used as a sonosensitizer for SDT. (a) Scheme of the synthetic procedure for Au-rGO-ZnO@PVP nanomaterials. (b) The mechanisms of Au-rGO-ZnO@PVP as a sonosensitizer for the generation of ROS to kill tumor cells and a catalyst for the production of O_2 to mitigate the hypoxic TME under ultrasound irradiation.

32.20%, respectively (Table S1 in the Electronic Supplementary Material (ESM)). Also, zeta potentials were used to determine the interaction between Au nanoparticles, ZnO nanoparticles, and rGO nanosheets. As shown in Fig. 2(f), the zeta potentials of rGO, ZnO, Au, and Au-rGO-ZnO were 16.81 ± 0.84, −31.40 ± 0.19, −26.32 ± 0.41, and −14.33 ± 0.52 mV, respectively. The considerable decrease in the zeta potential of rGO after integrated with ZnO nanoparticles and Au nanoparticles indicated the formation of Au-rGO-ZnO through electrostatic interaction. In Fig. 2(e), the characteristic peaks of GO are clearly viewed at 1,057 cm⁻¹ (alkoxy C–O stretching) and 1,720 cm⁻¹ (C=O stretching vibrations of carboxyl or carbonyl groups), but the intensity of these two IR peaks in both Au-rGO-ZnO and Au-rGO-ZnO@PVP decreased dramatically, which indicated GO has been reduced to rGO successfully [32, 33]. Furthermore, for enhancing the stability of Au-rGO-ZnO nanomaterials in physiological conditions, the Au-rGO-ZnO nanoparticles were enwrapped with PVP. As shown in Fig. 2(e), Au-rGO-ZnO@PVP nanomaterials exhibited a characteristic peak centered at 1,291 cm⁻¹ corresponding to the C–N stretch, indicating that Au-rGO-ZnO have been successfully functionalized with PVP [24]. Additionally, the thermogravimetric analysis (TGA) and the first derivative curves of Au-rGO-ZnO@PVP could also certificate the existence of PVP. In Fig. 2(g), there are three thermal events of Au-rGO-ZnO@PVP over the temperature range of 20–700 °C. Firstly, the mass loss from room temperature to 100 °C is due to the loss of water molecules existing on the surface. In the second stage, due to the thermal decomposition of unstable oxygen-containing functional groups remaining in rGO, roughly 7% mass loss takes place from 100 to 260 °C. Finally, in the range of 260–550 °C, about 30% mass loss corresponds to the decomposition of PVP in Au-rGO-ZnO@PVP. Moreover, Au-rGO-ZnO@PVP feature

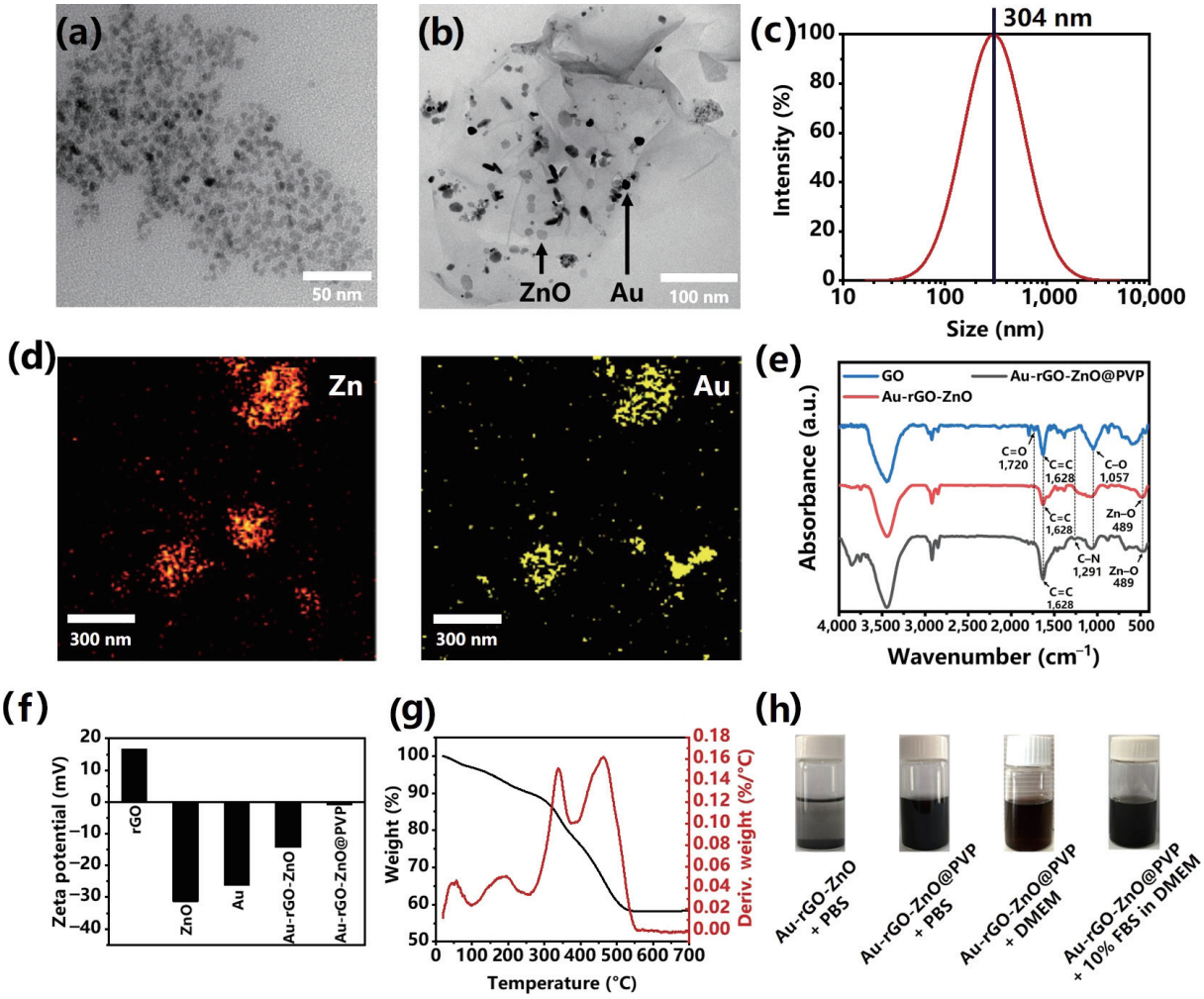

Figure 2 Characterization of Au-rGO-ZnO@PVP nanomaterials. (a) TEM image of highly dispersed ZnO nanoparticles. (b) TEM image of Au-rGO-ZnO@PVP nanomaterials. (c) Dynamic light scattering (DLS) size distribution profiles of Au-rGO-ZnO@PVP nanomaterials dispersed in aqueous solution. (d) SEM images of elemental mappings of Au-rGO-ZnO@PVP nanomaterials including Zn and Au elements. (e) FTIR spectra of GO nanosheets, Au-rGO-ZnO nanomaterials, and Au-rGO-ZnO@PVP nanomaterials. (f) Zeta potentials of rGO, ZnO, Au, Au-rGO-ZnO, and Au-rGO-ZnO@PVP. (g) TGA plots of Au-rGO-ZnO and Au-rGO-ZnO@PVP. (h) The images of Au-rGO-ZnO nanomaterials dispersed in PBS and Au-rGO-ZnO@PVP nanomaterials dispersed in PBS, DMEM, and 10% FBS in DMEM, respectively.

excellent stability in physiological solutions, such as PBS, DMEM, and DMEM containing 10% FBS (Fig. 2(h)).

3.2 Sonodynamic performance of Au-rGO-ZnO@PVP nanomaterials

The key role of rGO nanosheets in the Au-rGO-ZnO@PVP nanomaterials is to transfer generated electrons in ZnO upon ultrasound irradiation from ZnO to Au nanoparticles. Due to the electronic conductivity of rGO endowed with its π–π conjugated structure, the electrons generated in ZnO upon ultrasound irradiation can rapidly transfer from the conduction band of ZnO to rGO and from rGO to Au by a percolation mechanism, which could effectively inhibit electron–hole pair recombination [24, 34, 35], resulting in the generation of enough ROS, such as superoxide radical ($\cdot O_2^-$), ·OH, and $^1O_2$. To explore the ROS generation capability of Au-rGO-ZnO@PVP, DPBF and RhB were used as sensitive molecular probe to value the production of $^1O_2$, $\cdot O_2^-$, and ·OH, respectively [22, 36]. The generated $^1O_2$ reacted with DPBF, resulting in the decrease of its absorption intensity at about 420 nm in the UV–vis–NIR spectrums. From Fig. 3(a), the characteristic absorption of DPBF significantly reduced under the extension of ultrasound irradiation time in the solution with Au-rGO-ZnO@PVP while only slight absorbance decreases at 420 nm were observed in other control groups (ZnO) (Fig. 3(b) and Fig. S1 in the ESM), demonstrating that Au-rGO-ZnO@PVP system has good $^1O_2$ generation ability. Furthermore, the capability of ·OH production was characterized by RhB degradation assay. The absorption intensity of RhB (around 554 nm) displayed a rapid decrease within 4 min under ultrasound irradiation (1.0 MHz, 1.0 W/cm^2, 50% duty cycle), indicating the efficient ·OH generation by Au-rGO-ZnO@PVP (Fig. 3(c)). In contrast, no significant decline in absorption at 554 nm was observed in other groups (ZnO and ZnO-rGO@PVP) (Fig. 3(d) and Fig. S2 in the ESM). As shown in Figs. 3(b) and 3(d), Au-rGO-ZnO@PVP had the high capability of efficiently generating ROS during the US irradiation, which was about three times as much as ZnO nanoparticles. Furthermore, for investigating the effect of the loading amount of Au and ZnO on ROS generation, we have separately synthesized different nanomaterials, such as, Au-rGO@PVP, $Au_{0.5}$-rGO-ZnO@PVP, and Au-rGO-$ZnO_{0.5}$@PVP, and the mass ration of Au and ZnO in each nanomaterial is shown in Table S2 in the ESM. As shown in Fig. S3 in the ESM, the capability of Au-rGO-ZnO@PVP generating ROS was higher than other nanomaterials. Further, the results have verified ZnO as the main charge generating material and Au could also facilitate electrons transfer. For further investigating the ability of Au-rGO-ZnO@PVP to generate ROS, the formation of $^1O_2$ and ·OH was examined by ESR using TEMP and DMPO [37–39]. TEMP acting as a sensitive spin trap for $^1O_2$ can yield TEMPO which has a

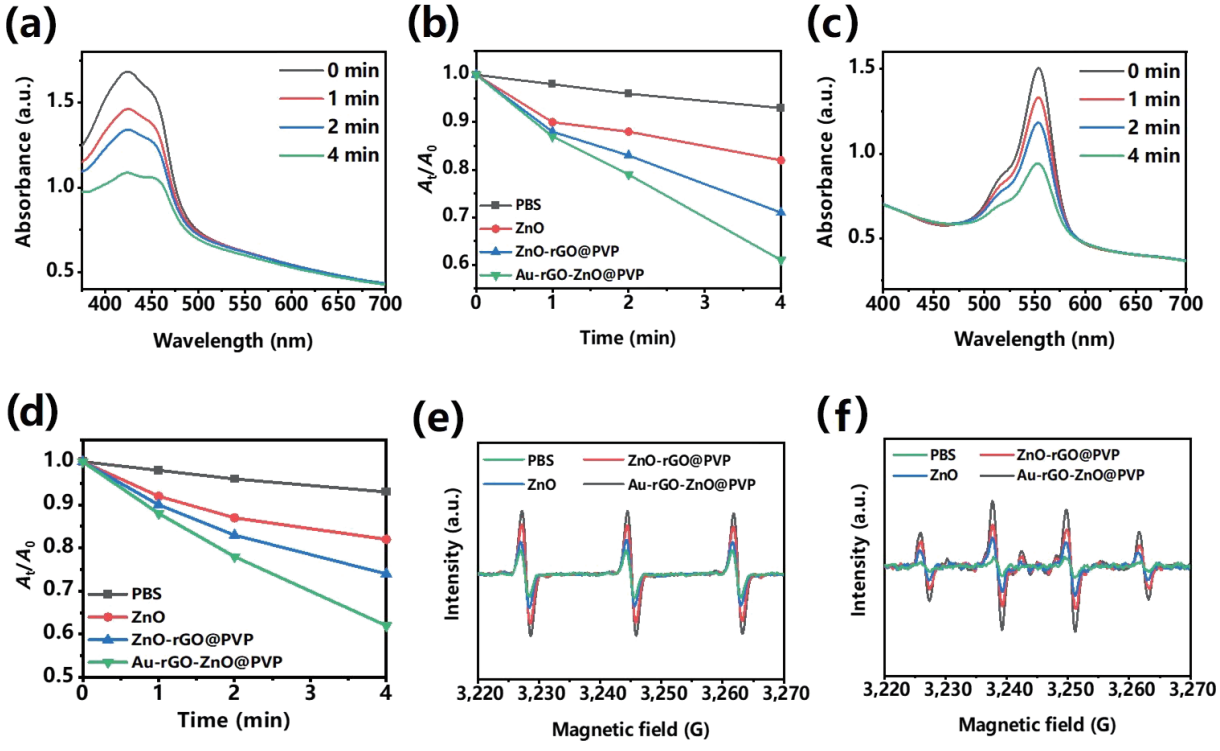

Figure 3 Son-catalytic performance of Au-rGO-ZnO@PVP. (a) UV–vis–NIR absorption spectra of the DPBF in the presence of Au-rGO-ZnO@PVP upon exposure to US irradiation. (b) Relative absorption of DPBF at 420 nm after coincubation with ZnO nanoparticles, ZnO-rGO@PVP nanomaterials, and Au-rGO-ZnO@PVP under different conditions. (c) UV–vis–NIR absorption spectra of the RhB in the presence of Au-rGO-ZnO@PVP upon exposure to US irradiation. (d) Relative absorption of RhB at 554 nm after coincubation with ZnO nanoparticles, ZnO-rGO@PVP, and Au-rGO-ZnO@PVP under different conditions. ESR spectra of (e) $^1O_2$ trapped by TEMP and (f) ·OH trapped by DMPO in ZnO, ZnO-rGO@PVP, and Au-rGO-ZnO@PVP dispersions after US irradiation. US irradiation: 1.0 MHz, 1.0 W/cm^2, 50% duty cycle.

characteristic 1:1:1 triple signal. Moreover, DMPO can make the ESR signal divide into a particular 1:2:2:1 quadruple peak by reacting with ·OH (Figs. 3(e) and 3(f)). The $^1O_2$ and ·OH characteristic signals of Au-rGO-ZnO@PVP were also almost three times as much as ZnO, which was similar as the characteristic absorption intensity of both DPBF and RhB. Furthermore, the PL spectra were used to demonstrate the recombination of the electrons and holes in Au-rGO-ZnO@PVP. As shown in Fig. S4 in the ESM, a broad luminescence peak could be observed in the region of 372–382 nm for all samples. Obviously, the PL intensity of ZnO decreased after combined with rGO. Moreover, the Au-rGO-ZnO@PVP showed much weaker PL intensity than ZnO and ZnO-rGO@PVP, indicating rGO could reduce the recombination of electrons and holes due to the ability of transferring electrons. Hence, compared with ZnO, the sono-catalytic performance of Au-rGO-ZnO@PVP has a considerable improvement, which is more conducive to the further SDT.

3.3 Oxygen production, extracellular and intracellular ROS production, and hypoxia mitigation

In view of the high metabolism of tumor and low blood perfusion, the tumor microenvironment is hypoxic, which restricts the generation of ROS during sonodynamic therapy. Hence, the presence of O_2 was critical to SDT [38, 40, 41]. It was reported that rGO integrated with Au nanoparticles could catalyze the decomposition of H_2O_2 to generate O_2 under US irradiation [26, 27]. To evaluate the capability of O_2 generation by Au-rGO-ZnO@PVP, we added H_2O_2 (50 μM) to simulate the H_2O_2-overexpressed tumor microenvironment in the intracellular experiments and also added H_2O_2 (1 mM) in the experiments. As shown in Fig. 4(a), there was almost no O_2 generation in the presence of Au-rGO-ZnO@PVP and H_2O_2 without US irradiation. Even under US irradiation, ZnO can hardly produce oxygen by catalyzing the decomposition of H_2O_2. However, due to the presence of rGO integrated with Au nanoparticles, the Au-rGO-ZnO@PVP can efficiently generate O_2 from H_2O_2 upon ultrasound irradiation, and the concentration of O_2 generation could be up to 10 mg/L in 150 s. In the meantime, the contribution of O_2 generation to enhance ROS quantum yield was also investigated. As shown in Fig. 4(b), the efficiency of ROS generation in the group Au-rGO-ZnO@PVP under hypoxic environment upon US irradiation was only about half of the group Au-rGO-ZnO@PVP in normoxic condition. Furthermore, $Ru(dpp)_3Cl_2$ was used to explore whether Au-rGO-ZnO@PVP could enhance the oxygen production in both HeLa and CT26 cells or not in both hypoxic and normoxic environment [42]. $Ru(dpp)_3Cl_2$ emits red fluorescence, which is quenched by the presence of O_2. Firstly, the dependent manner of H_2O_2 treatment in time and concentration is shown in Fig. S5 in the ESM, and the concentration of H_2O_2 as 50 μM was chose in the subsequent experiments. As shown in Fig. 4(c) and Fig. S6(a) in the ESM, in the hypoxic environment, the red fluorescence of $Ru(dpp)_3Cl_2$ in both HeLa and CT26 cells in the Au-rGO-ZnO@PVP + H_2O_2 + US group quenched completely, while the Au-rGO-ZnO@PVP + US and Au-rGO-ZnO@PVP + H_2O_2 groups still emerged strong red fluorescence, which indicated Au-rGO-ZnO@PVP can mitigate the hypoxia tumor microenvironment effectively by efficiently alternating the overexpressed H_2O_2 to O_2 under US irradiation. The ROS generation efficiency in both HeLa and CT26 cells under different conditions was evaluated by DCFH-DA, which can rapidly react with ROS and convert into 2,7-dichlorofluorescein (DCF) with strong green fluorescence [37, 43]. As shown in Fig. 4(d) and Fig. S6(b) in the ESM, under US irradiation, the intensity of green fluorescence in the group Au-rGO-ZnO@PVP + H_2O_2 in the hypoxic environment was much

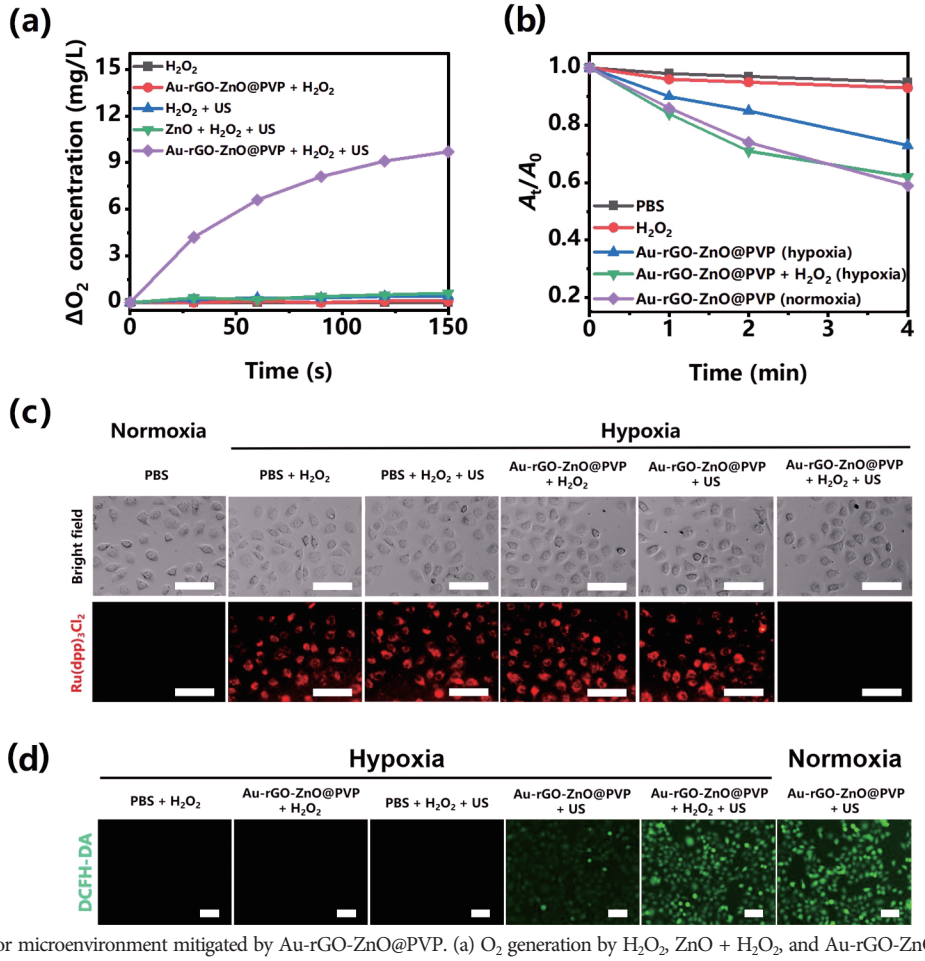

Figure 4 Hypoxia tumor microenvironment mitigated by Au-rGO-ZnO@PVP. (a) O_2 generation by H_2O_2, ZnO + H_2O_2, and Au-rGO-ZnO@PVP + H_2O_2 with or without US irradiation. (b) Relative absorption of DPBF at 420 nm under different conditions. The concentration of H_2O_2 was 1 mM. (c) Fluorescence images of Ru(dpp)$_3$Cl$_2$-stained HeLa cells after different treatments. (d) Fluorescence images of HeLa cells stained by DCFH-DA after various treatments in hypoxic and normoxic environment. All scale bars represent 200 μm. The concentration of H_2O_2 was 50 μM. US irradiation: 1.0 MHz, 1.0 W/cm^2, 50% duty cycle.

stronger than the group Au-rGO-ZnO@PVP only and almost the same as the group Au-rGO-ZnO@PVP under normoxic condition, demonstrating that Au-rGO-ZnO@PVP have the potential to further enhance the ROS generation efficiency of SDT by mitigating the hypoxia tumor environment effectively [13, 14, 44]. Furthermore, as shown in Fig. S9(a) in the ESM, the result of fluorescence activated cell sorting (FACS) was also consistent with the fluorescence images of DCFH-DA staining.

3.4 *In vitro* sonodynamic therapy against tumor cells

The cytotoxicity of Au-rGO-ZnO@PVP nanomaterials *in vitro* was measured through MTT assay by using tumor cells (HeLa, CT26, and 4T1 cells) and normal cells (L929 cells), separately. These cells were incubated with Au-rGO-ZnO@PVP at different concentrations (12.5, 25, 50, 75, and 100 μg/mL) for 24 h. Cell viabilities were still above 90% at concentrations as high as 75 μg/mL without US irradiation, indicating the biocompatibility and the negligible cytotoxicity of Au-rGO-ZnO@PVP (Fig. 5(a) and Fig. S7 in the ESM). We evaluated the cytotoxicity of ZnO in both HeLa cells and CT26 cells under US irradiation (1.0 MHz, 1.0 W/cm^2, 50% duty cycle, 2 min), and the results showed that ZnO did not exhibit significant cytotoxicity under US irradiation (Fig. 5(b) and Fig. S8(a) in the ESM), which may result from the fact that the separated electrons and holes produced by ZnO under US could easily recombine, preventing enough ROS production to kill cancer cells. Since rGO has high ability to transfer electrons and rGO bridges ZnO and Au nanoparticles in Au-rGO-ZnO@PVP, the separated electrons produced in Au-rGO-ZnO@PVP under US irradiation could be easily transferred from ZnO to rGO to Au nanoparticles, highly inhibiting the recombination of the separated e^-–h^+ and facilitating ROS production to effectively kill cancer cells [45, 46]. We also used DCFH-DA staining assay to trace the intracellular ROS generation at different conditions (Fig. 5(d) and Fig. S8(c) in the ESM). It is obvious that the ROS generation using Au-rGO-ZnO@PVP was much higher than that using ZnO and ZnO-rGO@PVP under US irradiation. The further FACS was also consistent with the DCFH-DA fluorescence staining where the Au-rGO-ZnO@PVP + US group has the highest intracellular green-fluorescence intensity (Fig. S9(b) in the ESM). In the *in vitro* experiment, it was found that the efficiency of SDT against cancer cells using Au-rGO-ZnO@PVP was positively correlated with the power and time of US irradiation (Fig. 5(c) and Fig. S8(b) in the ESM). Both the HeLa cells and CT26 cells co-incubated with Au-rGO-ZnO@PVP (50 μg/mL) almost lost vitality under US irradiation (1.0 MHz, 1.5 W/cm^2, 50% duty cycle, 3min). Moreover, as shown in Fig. S10 in the ESM, the Au-rGO-ZnO@PVP also have high activity against U373MG cells (half maximum inhibitory concentration (IC_{50}) = 28 μg/mL) under US irradiation. Furthermore, the cytotoxicity of different treatment was detected through staining the live and dead cells with Calcein-AM and PI, observing the live cells (green fluorescence) and dead cells (red fluorescence) (Fig. 5(e) and Fig. S8(d) in the ESM). From the ZnO with US irradiation group, about 70% of cells illustrated green fluorescence, indicating very limited therapy results. However, after co-incubated with Au-rGO-ZnO@PVP and exposed to US treatment, most of cells died exhibiting strong red fluorescence. This convincingly revealed that Au-rGO-ZnO@PVP can efficiently enhance SDT compared with the ZnO nanoparticles.

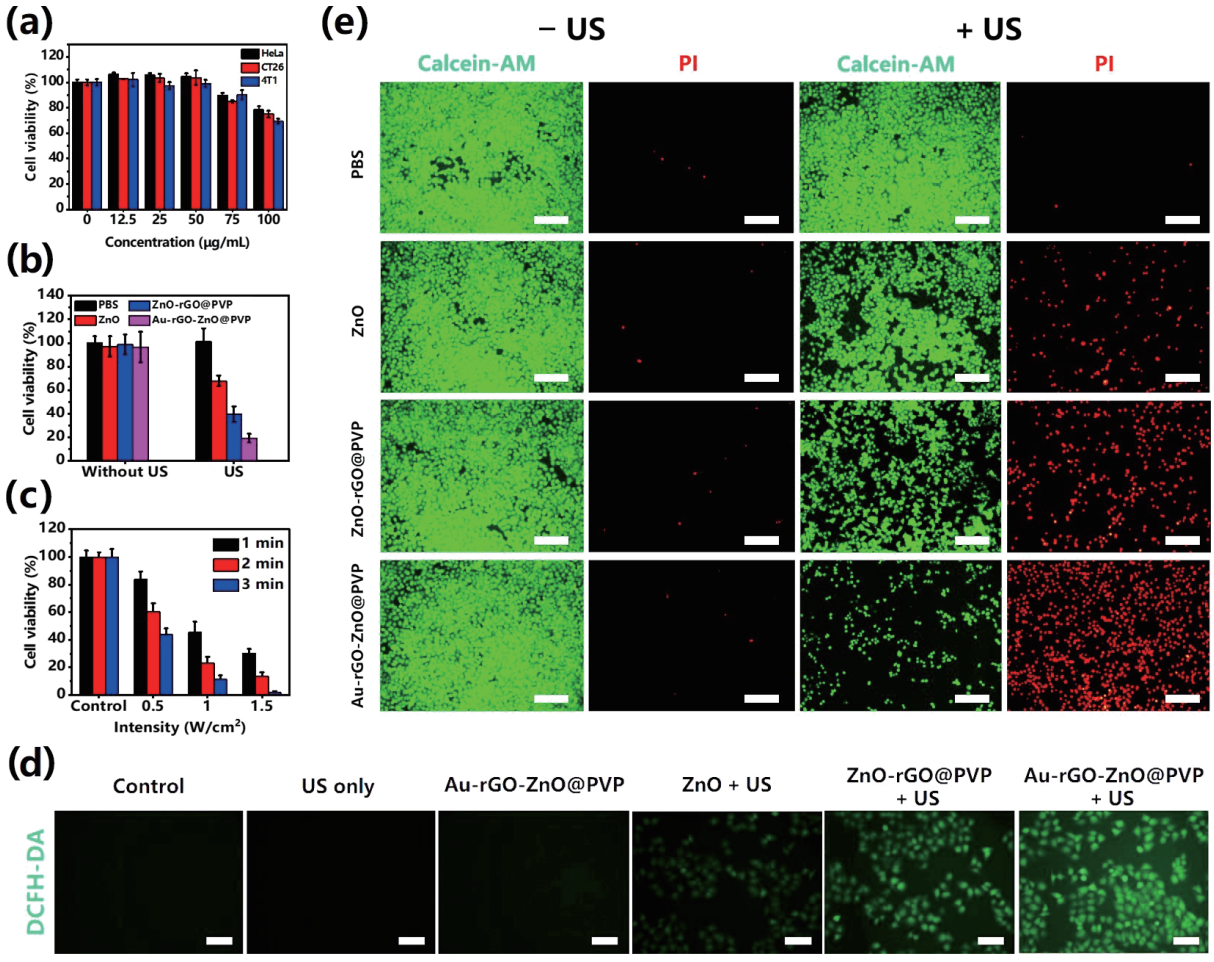

Figure 5 *In vitro* SDT using Au-rGO-ZnO@PVP. (a) The viabilities of HeLa, CT26, and 4T1 cells after being co-incubated with different concentrations of Au-rGO-ZnO@PVP for 24 h. (b) The viabilities of HeLa cells after different treatments, including PBS only, ZnO, ZnO-rGO@PVP, and Au-rGO-ZnO@PVP with or without US irradiation. (c) The viabilities of HeLa cells after incubation with Au-rGO-ZnO@PVP under different conditions, including elevated US power densities and prolonged US irradiation durations. (d) Fluorescence images of HeLa cells stained by DCFH-DA after different treatments (scale bars represent 200 μm). (e) Fluorescence images of HeLa cells stained by Calcein AM/PI after different treatments. Green signal represents live cells; red signal represents dead cells; scale bars represent 500 μm. US irradiation: 1.0 MHz, 1.0 W/cm^2, 50% duty cycle.

3.5 *In vivo* sonodynamic therapy on tumor cells by Au-rGO-ZnO@PVP

To evaluate the tumor therapy efficiency of the Au-rGO-ZnO@PVP *in vivo*, the CT26 tumors bearing mice were randomly divided into six groups: PBS, Au-rGO-ZnO@PVP only, US only, ZnO + US, ZnO-rGO@PVP + US, and Au-rGO-ZnO@PVP + US. After intratumorally injected with PBS, ZnO, ZnO-rGO@PVP, and Au-rGO-ZnO@PVP for 1 h, the mice were irradiated with US (1.0 MHz, 1.0 W/cm^2, 50% duty cycle) for 4 min and repeated on the fourth day during the therapeutic process (Fig. 6(a)). For testing the *in vivo* biocompatibility assays of Au-rGO-ZnO@PVP nanomaterials, we have performed comprehensive experiments on healthy female Balb/c mice. Firstly, excellent biocompatibility was reflected in no hemolysis in hemolysis experiments (Fig. S11 in the ESM). Meanwhile, we used blood panel analysis and blood biochemistry test to further describe the excellent biocompatibility of Au-rGO-ZnO@PVP nanomaterials (Fig. S12 in the ESM). Furthermore, during 14 days of the treatment, the body weight of mice had no obvious change among all the groups, demonstrating no serious side effects of the Au-rGO-ZnO@PVP (Fig. 6(b)). As shown in Fig. 6(c), the groups treated with PBS showed a rapid increase in the tumor size with or without US irradiation. Au-rGO-ZnO@PVP also failed to inhibit tumor growth without US irradiation, and the tumor volumes of mice increased by about 20 times after 14 days. Under US irradiation, ZnO alone could not suppress tumor growth, and tumor volumes increased by 10 times after 14 days of therapy. However, the tumor volumes of mice injected with Au-rGO-ZnO@PVP under US irradiation declined slowly.

The tumor inhibition rate of the Au-rGO-ZnO@PVP + US group reached up to 97%, which was much higher than the tumor inhibition rate of other groups (Fig. S13 in the ESM). Moreover, the results also have shown that the survival rates of these mice injected with Au-rGO-ZnO@PVP and ZnO-rGO@PVP were over 90% under US irradiation. However, all mice treated with US only and ZnO + US died after 50 days, which indicated the remarkable anti-tumor efficiency of Au-rGO-ZnO@PVP under US irradiation (Fig. 6(d)). Mice were sacrificed on day 14 and the photo of the excised tumors (Fig. 6(e)) from the mice demonstrated that Au-rGO-ZnO@PVP could highly inhibit tumor proliferation due to enhanced SDT. *In vivo* ROS staining of tumor slices was conducted to evaluate the ROS level in tumor. Compared with other groups, Au-rGO-ZnO@PVP + US group showed the highest green fluorescence, which was much stronger than ZnO + US group, indicating Au-rGO-ZnO@PVP could generate more ROS under US irradiation (Fig. S14 in the ESM). Finally, tumor tissue was stained with H&E and TUNEL to value the sonodynamic therapeutic effect of Au-rGO-ZnO@PVP (Fig. 6(f)). The H&E staining revealed that neither Au-rGO-ZnO@PVP only group nor US only group led to cell death in the tumor areas and the typical TUNEL staining displayed the maximum apoptosis

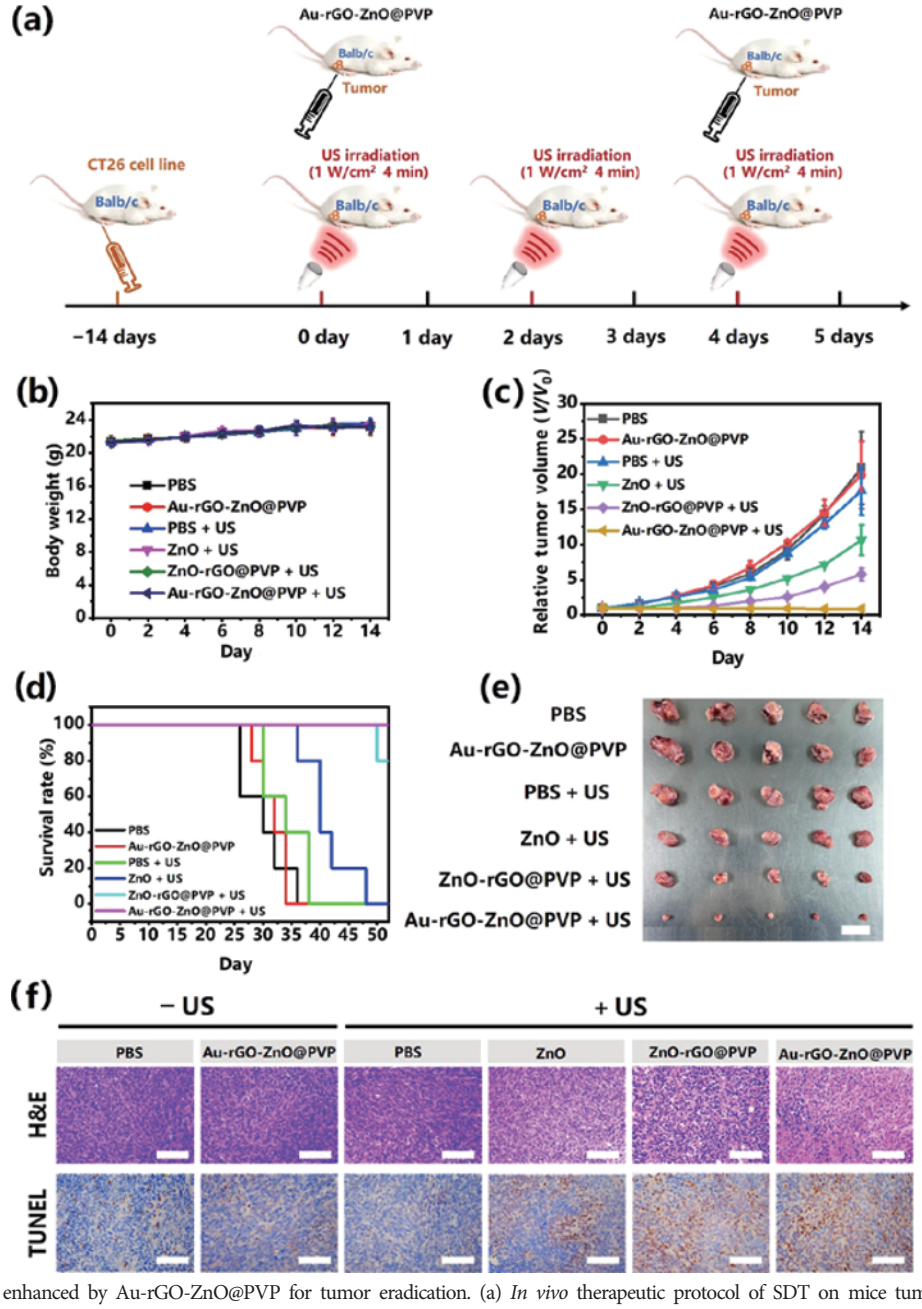

Figure 6 *In vivo* SDT enhanced by Au-rGO-ZnO@PVP for tumor eradication. (a) *In vivo* therapeutic protocol of SDT on mice tumor xenograft. (b) Time-dependent body–weight curves of CT26 tumor-bearing mice after different treatments. (c) Survival curves of the CT26 tumor-bearing mice in different groups. (d) Tumor growth curves of different groups of the CT26 tumor-bearing mice after various treatments. (e) The images of tumors after different treatment (scale bars represent 3 cm). (f) H&E and TUNEL staining of tumor tissues in different groups (scale bars represent 200 μm). US irradiation: 1.0 MHz, 1.0 W/cm², 50% duty cycle.

and necrosis for the Au-rGO-ZnO@PVP + US group. As with the tumor growth curve, both the H&E staining and the TUNEL staining images displayed that tumors treated with Au-rGO-ZnO@PVP under US irradiation exhibited the most severe tumor tissue damage and cell necrosis, which indicates the Au-rGO-ZnO@PVP can suppress tumor effectively due to the enhanced SDT [21, 47–49]. In addition, no obvious organ damage or inflammation was observed in different group according to the H&E staining of organs collected at day 14 (Fig. S15 in the ESM).

4 Conclusions

In summary, we have successfully constructed an excellent sonosensitizer, Au-rGO-ZnO@PVP, via integrating ZnO nanoparticles and Au nanoparticles on the rGO nanosheet. The rGO in the system can effectively promote rapid electron transference from ZnO to Au nanoparticles, which highly inhibits the recombination of e^-–h^+ pairs generated in ZnO under US irradiation, highly promoting the production of ROS and enhancing the efficiency of SDT in return. Furthermore, rGO integrated with Au nanoparticles could act as an effective catalyst to promote the generation O_2 from endogenous H_2O_2, which could improve the hypoxic tumor microenvironment effectively under US irradiation to further enhance therapeutic efficiency. The results have shown that the designed Au-rGO-ZnO@PVP has high ability to kill tumor under US irradiation, and the tumor inhibition rate is much higher than that of ZnO. This work provides a promising strategy to design an efficient inorganic sonosensitizer for enhanced sonodynamic therapy by promoting electrons transfer and O_2 generation.

Acknowledgements

We acknowledge founding support from the National Key R&D program of China (Nos. 2017YFA0205600 and 2020YFA0710700), the National Science Funds for Distinguished

Yong Scholars (No. 51625305), the National Natural Science Foundation of China (Nos. 52131305, 52073269, 51873202, 22131010, 22101275, 81603339, 81602344, and 31870993), and the Fundamental Research Funds for the Central Universities (Nos. YD2060002016 and WK9110000005).

Electronic Supplementary Material: Supplementary material (the UV–vis–NIR absorption spectra of the DPBF and the RhB, biological effect assessment of the Au-rGO-ZnO@PVP, and the inhibition rate of tumor under different treatments during the animal study) is available in the online version of this article at https://doi.org/10.1007/s12274-022-4599-5.

References

[1] Grivennikov, S. I.; Greten, F. R.; Karin, M. Immunity, inflammation, and cancer. *Cell* **2010**, *140*, 883–899.

[2] Zhou, Z. J.; Song, J. B.; Nie, L. M.; Chen, X. Y. Reactive oxygen species generating systems meeting challenges of photodynamic cancer therapy. *Chem. Soc. Rev.* **2016**, *45*, 6597–6626.

[3] Liu, J. T.; Zhang, L.; Lei, J. P.; Shen, H.; Ju, H. X. Multifunctional metal-organic framework nanoprobe for cathepsin b-activated cancer cell imaging and chemo-photodynamic therapy. *ACS Appl. Mater. Interfaces* **2017**, *9*, 2150–2158.

[4] Zhu, Y.; Shi, H. D.; Li, T. W.; Yu, J. N.; Guo, Z. X.; Cheng, J. J.; Liu, Y. Z. A dual functional nanoreactor for synergistic starvation and photodynamic therapy. *ACS Appl. Mater. Interfaces* **2020**, *12*, 18309–18318.

[5] He, G. L.; Xu, N.; Ge, H. Y.; Lu, Y.; Wang, R.; Wang, H. X.; Du, J. J.; Fan, J. L.; Sun, W.; Peng, X. J. Red-light-responsive Ru complex photosensitizer for lysosome localization photodynamic therapy. *ACS Appl. Mater. Interfaces* **2021**, *13*, 19572–19580.

[6] Zhong, S.; Chen, C.; Yang, G. L.; Zhu, Y. C.; Cao, H. L.; Xu, B. J.; Luo, Y. Q.; Gao, Y.; Zhang, W. A. Acid-triggered nanoexpansion polymeric micelles for enhanced photodynamic therapy. *ACS Appl. Mater. Interfaces* **2019**, *11*, 33697–33705.

[7] Liu, C. H.; Dong, H. F.; Wu, N. Q.; Cao, Y.; Zhang, X. J. Plasmonic resonance energy transfer enhanced photodynamic therapy with Au@SiO_2@Cu_2O/perfluorohexane nanocomposites. *ACS Appl. Mater. Interfaces* **2018**, *10*, 6991–7002.

[8] Zhang, Y.; Wang, F. M.; Liu, C. Q.; Wang, Z. Z.; Kang, L. H.; Huang, Y. Y.; Dong, K.; Ren, J. S.; Qu, X. G. Nanozyme decorated metal-organic frameworks for enhanced photodynamic therapy. *ACS Nano* **2018**, *12*, 651–661.

[9] Agostinis, P.; Berg, K.; Cengel, K. A.; Foster, T. H.; Girotti, A. W.; Gollnick, S. O.; Hahn, S. M.; Hamblin, M. R.; Juzeniene, A.; Kessel, D. et al. Photodynamic therapy of cancer: An update. *CA Cancer J. Clin.* **2011**, *61*, 250–281.

[10] Tang, H. L.; Zheng, Y. Y.; Chen, Y. Materials chemistry of nanoultrasonic biomedicine. *Adv. Mater.* **2017**, *29*, 1604105.

[11] Qian, X. Q.; Zheng, Y. Y.; Chen, Y. Micro/nanoparticle-augmented sonodynamic therapy (SDT): Breaking the depth shallow of photoactivation. *Adv. Mater.* **2016**, *28*, 8097–8129.

[12] Pan, X. T.; Bai, L. X.; Wang, H.; Wu, Q. Y.; Wang, H. Y.; Liu, S.; Xu, B. L.; Shi, X. H.; Liu, H. Y. Metal-organic-framework-derived carbon nanostructure augmented sonodynamic cancer therapy. *Adv. Mater.* **2018**, *30*, 1800180.

[13] Zhu, P.; Chen, Y.; Shi, J. L. Nanoenzyme-augmented cancer sonodynamic therapy by catalytic tumor oxygenation. *ACS Nano* **2018**, *12*, 3780–3795.

[14] Chen, H. J.; Zhou, X. B.; Gao, Y.; Zheng, B. Y.; Tang, F. X.; Huang, J. D. Recent progress in development of new sonosensitizers for sonodynamic cancer therapy. *Drug Discov. Today* **2014**, *19*, 502–509.

[15] Feng, Q. H.; Zhang, W. X.; Yang, X. M.; Li, Y. Z.; Hao, Y. W.; Zhang, H. L.; Hou, L.; Zhang, Z. Z. pH/ultrasound dual-responsive gas generator for ultrasound imaging-guided therapeutic inertial cavitation and sonodynamic therapy. *Adv. Healthc. Mater.* **2018**, *7*, 1700957.

[16] Sun, D.; Pang, X.; Cheng, Y.; Ming, J.; Xiang, S. J.; Zhang, C.; Lv, P.; Chu, C. C.; Chen, X. L.; Liu, G. et al. Ultrasound-switchable nanozyme augments sonodynamic therapy against multidrug-resistant bacterial infection. *ACS Nano* **2020**, *14*, 2063–2076.

[17] Ma, A. Q.; Chen, H. Q.; Cui, Y. H.; Luo, Z. Y.; Liang, R. J.; Wu, Z. H.; Chen, Z.; Yin, T.; Ni, J.; Zheng, M. B. et al. Metalloporphyrin complex-based nanosonosensitizers for deep-tissue tumor theranostics by noninvasive sonodynamic therapy. *Small* **2019**, *15*, 1804028.

[18] Cao, Y.; Wu, T. T.; Dai, W. H.; Dong, H. F.; Zhang, X. J. TiO_2 nanosheets with the Au nanocrystal-decorated edge for mitochondria-targeting enhanced sonodynamic therapy. *Chem. Mater.* **2019**, *31*, 9105–9114.

[19] Deepagan, V. G.; You, D. G.; Um, W.; Ko, H.; Kwon, S.; Choi, K. Y.; Yi, G. R.; Lee, J. Y.; Lee, D. S.; Kim, K. et al. Long-circulating Au-TiO_2 nanocomposite as a sonosensitizer for ROS-mediated eradication of cancer. *Nano Lett.* **2016**, *16*, 6257–6264.

[20] Son, S.; Kim, J. H.; Wang, X. W.; Zhang, C. L.; Yoon, S. A.; Shin, J.; Sharma, A.; Lee, M. H.; Cheng, L.; Wu, J. S. et al. Multifunctional sonosensitizers in sonodynamic cancer therapy. *Chem. Soc. Rev.* **2020**, *49*, 3244–3261.

[21] Wang, X. W.; Zhong, X. Y.; Bai, L. X.; Xu, J.; Gong, F.; Dong, Z. L.; Yang, Z. J.; Zeng, Z. J.; Liu, Z.; Cheng, L. Ultrafine titanium monoxide (TiO_{1+x}) nanorods for enhanced sonodynamic therapy. *J. Am. Chem. Soc.* **2020**, *142*, 6527–6537.

[22] Liang, S.; Deng, X. R.; Xu, G. Y.; Xiao, X.; Wang, M. F.; Guo, X. S.; Ma, P. A.; Cheng, Z. Y.; Zhang, D.; Lin, J. A novel Pt-TiO_2 heterostructure with oxygen-deficient layer as bilaterally enhanced sonosensitizer for synergistic chemo-sonodynamic cancer therapy. *Adv. Funct. Mater.* **2020**, *30*, 1908598.

[23] Liu, Y.; Wang, Y.; Zhen, W. Y.; Wang, Y. H.; Zhang, S. T.; Zhao, Y.; Song, S. Y.; Wu, Z. J.; Zhang, H. J. Defect modified zinc oxide with augmenting sonodynamic reactive oxygen species generation. *Biomaterials* **2020**, *251*, 120075.

[24] Dai, C.; Zhang, S. J.; Liu, Z.; Wu, R.; Chen, Y. Two-dimensional graphene augments nanosonosensitized sonocatalytic tumor eradication. *ACS Nano* **2017**, *11*, 9467–9480.

[25] Xu, H. Y.; Zhang, X.; Han, R. B.; Yang, P. M.; Ma, H. F.; Song, Y.; Lu, Z. C.; Yin, W. D.; Wu, X. X.; Wang, H. Nanoparticles in sonodynamic therapy: State of the art review. *RSC Adv.* **2016**, *6*, 50697–50705.

[26] He, W. W.; Zhou, Y. T.; Wamer, W. G.; Hu, X. N.; Wu, X. C.; Zheng, Z.; Boudreau, M. D.; Yin, J. J. Intrinsic catalytic activity of Au nanoparticles with respect to hydrogen peroxide decomposition and superoxide scavenging. *Biomaterials* **2013**, *34*, 765–773.

[27] Tao, Y.; Lin, Y. H.; Huang, Z. Z.; Ren, J. S.; Qu, X. G. Incorporating graphene oxide and gold nanoclusters: A synergistic catalyst with surprisingly high peroxidase-like activity over a broad ph range and its application for cancer cell detection. *Adv. Mater.* **2013**, *25*, 2594–2599.

[28] Aboulaich, A.; Tilmaciu, C. M.; Merlin, C.; Mercier, C.; Guilloteau, H.; Medjahdi, G.; Schneider, R. Physicochemical properties and cellular toxicity of (poly)aminoalkoxysilanes-functionalized ZnO quantum dots. *Nanotechnology* **2012**, *23*, 335101.

[29] Chen, Z. W.; Li, Z. H.; Wang, J. S.; Ju, E. G.; Zhou, L.; Ren, J. S.; Qu, X. G. A multi-synergistic platform for sequential irradiation-activated high-performance apoptotic cancer therapy. *Adv. Funct. Mater.* **2014**, *24*, 522–529.

[30] Wang, C. C.; Shieu, F. S.; Shih, H. C. Enhanced photodegradation by RGO/ZnO core-shell nanostructures. *J. Environ. Chem. Eng.* **2020**, *8*, 103589.

[31] Roy, P.; Periasamy, A. P.; Liang, C. T.; Chang, H. T. Synthesis of graphene-ZnO-Au nanocomposites for efficient photocatalytic reduction of nitrobenzene. *Environ. Sci. Technol.* **2013**, *47*, 6688–6695.

[32] Kim, S. H.; Lee, J. E.; Sharker, S. M.; Jeong, J. H.; In, I.; Park, S. Y. *In vitro* and *in vivo* tumor targeted photothermal cancer therapy using functionalized graphene nanoparticles. *Biomacromolecules* **2015**, *16*, 3519–3529.

[33] Lv, K. L.; Fang, S.; Si, L. L.; Xia, Y.; Ho, W.; Li, M. Fabrication of

TiO_2 nanorod assembly grafted rGO (rGO@TiO_2-NR) hybridized flake-like photocatalyst. *Appl. Surf. Sci.* **2017**, *391*, 218–227.

[34] Li, Q.; Guo, B. D.; Yu, J. G.; Ran, J. R.; Zhang, B. H.; Yan, H. J.; Gong, J. R. Highly efficient visible-light-driven photocatalytic hydrogen production of CdS-cluster-decorated graphene nanosheets. *J. Am. Chem. Soc.* **2011**, *133*, 10878–10884.

[35] Wang, P. F.; Zhan, S. H.; Xia, Y. G.; Ma, S. L.; Zhou, Q. X.; Li, Y. The fundamental role and mechanism of reduced graphene oxide in rGO/Pt-TiO_2 nanocomposite for high-performance photocatalytic water splitting. *Appl. Catal. B Environ.* **2017**, *207*, 335–346.

[36] Zhang, W. J.; Hu, X. L.; Shen, Q.; Xing, D. Mitochondria-specific drug release and reactive oxygen species burst induced by polyprodrug nanoreactors can enhance chemotherapy. *Nat. Commun.* **2019**, *10*, 1704.

[37] Zhu, W. J.; Chen, Q.; Jin, Q. T.; Chao, Y.; Sun, L. L.; Han, X.; Xu, J.; Tian, L. L.; Zhang, J. L.; Liu, T. et al. Sonodynamic therapy with immune modulatable two-dimensional coordination nanosheets for enhanced anti-tumor immunotherapy. *Nano Res.* **2021**, *14*, 212–221.

[38] Pan, X. T.; Wang, W. W.; Huang, Z. J.; Liu, S.; Guo, J.; Zhang, F. R.; Yuan, H. J.; Li, X.; Liu, F. Y.; Liu, H. Y. MOF-derived double-layer hollow nanoparticles with oxygen generation ability for multimodal imaging-guided sonodynamic therapy. *Angew. Chem., Int. Ed.* **2020**, *59*, 13557–13561.

[39] Chen, W.; Liu, C.; Ji, X. Y.; Joseph, J.; Tang, Z. M.; Ouyang, J.; Xiao, Y. F.; Kong, N.; Joshi, N.; Farokhzad, O. C. et al. Stanene-based nanosheets for β-elemene delivery and ultrasound-mediated combination cancer therapy. *Angew. Chem., Int. Ed.* **2021**, *60*, 7155–7164.

[40] Li, G. Z.; Wang, S. P.; Deng, D. S.; Xiao, Z. S.; Dong, Z. L.; Wang, Z. P.; Lei, Q. F.; Gao, S.; Huang, G. X.; Zhang, E. P. et al. Fluorinated chitosan to enhance transmucosal delivery of sonosensitizer-conjugated catalase for sonodynamic bladder cancer treatment post-intravesical instillation. *ACS Nano* **2020**, *14*, 1586–1599.

[41] Ouyang, J.; Tang, Z. M.; Farokhzad, N.; Kong, N.; Kim, N. Y.; Feng, C.; Blake, S.; Xiao, Y. F.; Liu, C.; Xie, T. et al. Ultrasound mediated therapy: Recent progress and challenges in nanoscience. *Nano Today* **2020**, *35*, 100949.

[42] Lei, B.; Li, B.; Zhang, H.; Lu, S.; Zheng, Z.; Li, W.; Wang, Y. Mesostructured silica chemically doped with Ru^{II} as a superior optical oxygen sensor. *Adv. Funct. Mater.* **2006**, *16*, 1883–1891.

[43] Zhu, W. J.; Yang, Y.; Jin, Q. T.; Chao, Y.; Tian, L. L.; Liu, J. J.; Dong, Z. L.; Liu, Z. Two-dimensional metal-organic-framework as a unique theranostic nano-platform for nuclear imaging and chemo-photodynamic cancer therapy. *Nano Res.* **2019**, *12*, 1307–1312.

[44] Costley, D.; Mc Ewan, C.; Fowley, C.; McHale, A. P.; Atchison, J.; Nomikou, N.; Callan, J. F. Treating cancer with sonodynamic therapy: A review. *Int. J. Hyperthermia* **2015**, *31*, 107–117.

[45] Wang, C.; Cao, F. J.; Ruan, Y. D.; Jia, X. D.; Zhen, W. Y.; Jiang, X. E. Specific generation of singlet oxygen through the russell mechanism in hypoxic tumors and GSH depletion by Cu-TCPP nanosheets for cancer therapy. *Angew. Chem., Int. Ed.* **2019**, *58*, 9846–9850.

[46] Liang, S.; Deng, X. R.; Chang, Y.; Sun, C. Q.; Shao, S.; Xie, Z. X.; Xiao, X.; Ma, P.; Zhang, H. Y.; Cheng, Z. Y. et al. Intelligent hollow Pt-CuS janus architecture for synergistic catalysis-enhanced sonodynamic and photothermal cancer therapy. *Nano Lett.* **2019**, *19*, 4134–4145.

[47] Yue, W. W.; Chen, L.; Yu, L. D.; Zhou, B. G.; Yin, H. H.; Ren, W. W.; Liu, C.; Guo, L. H.; Zhang, Y. F.; Sun, L. P. et al. Checkpoint blockade and nanosonosensitizer-augmented noninvasive sonodynamic therapy combination reduces tumour growth and metastases in mice. *Nat. Commun.* **2019**, *10*, 2025.

[48] Maisonnasse, P.; Guedj, J.; Contreras, V.; Behillil, S.; Solas, C.; Marlin, R.; Naninck, T.; Pizzorno, A.; Lemaitre, J.; Gonçalves, A. et al. Hydroxychloroquine use against SARS-CoV-2 infection in non-human primates. *Nature* **2020**, *585*, 584–587.

[49] Wang, Z. Z.; Zhang, Y.; Ju, E. G.; Liu, Z.; Cao, F. F.; Chen, Z. W.; Ren, J. S.; Qu, X. G. Biomimetic nanoflowers by self-assembly of nanozymes to induce intracellular oxidative damage against hypoxic tumors. *Nat. Commun.* **2018**, *9*, 3334.